

Helicity Density Enhancement in a Planar Array of Achiral High-Density Dielectric Nanoparticles

Mina Hanifeh¹ and Filippo Capolino²

Department of Electrical Engineering and Computer Science, University of California, Irvine, California 92697, USA

ABSTRACT

We propose a way to enhance electromagnetic field's helicity density of a circularly polarized plane wave based on its interaction with a layer composed of a planar periodic array of resonant achiral high-refractive index dielectric nanoparticles. The array generates a surface distribution of helicity density that everywhere has the same handedness of the exciting plane wave. Such a property is useful to interact with chiral samples like a layer of chiral molecules and can be used to improve chirality detection, paving the way to chirality detection with circular dichroism (CD) at surface level instead of in the bulk. Importantly, since the proposed array is composed of achiral inclusions it does not contribute by itself to the observed CD signal, and hence, it eliminates the need to separate the CD signal of the array and the chiral sample, in detecting the sample's chirality.

I. INTRODUCTION

Chirality means lack of any plane of symmetry or inversion center, and chiral objects are not superimposed on their mirror images^{1,2}. Chirality is an outspread geometrical property: from helical orbitals of planets around the Sun to snail shells. It is also observed in building blocks of life, i.e., molecules^{3,4}. Although many of natural molecules are found with one handedness, artificial substances which have become an indispensable part of our lives (e.g. medicines) mostly contain both enantiomers¹. Conflicting effects of enantiomers on our bodies necessitate the separation of enantiomers and investigation of their properties^{1,3}.

There has been extensive research on determining handedness and strength of chirality in chiral materials⁵⁻¹⁷. One method is circular dichroism (CD) where transmitted powers of circularly polarized plane waves with opposite handedness through a layer of chiral medium with a thickness d are used to reveal the material's chirality¹². In 2010, it was suggested that replacing plane waves by structured lights with high helicity density improves chirality detection^{5,6}. Subsequently, nearfields of various nanoantennas (NA) were proposed to enhance helicity in their nearfields^{13,14,18-21}. In recent CD experiments, a chiral layer is deposited on an array of chiral plasmonic structures to enhance detection (see e.g., Refs. ^{7,22}). However, the handedness of fields around plasmonic structures alternates²³⁻²⁵,

and an array of elements with uniform (or quasi uniform) distribution of helicity density with *same* handedness has never been proposed, which is indeed the goal of this paper. Here, we first show that a spherical high-density dielectric nanoantenna (DNA) (made for example of Silicon or TiO₂) generates azimuthally symmetric helicity density in the transverse plane with respect to the propagation direction of the incident field, when illuminated by a circularly polarized plane wave (see Ref. ¹⁵). We then implement such a DNA as a building block to design a surface made of a dense planar periodic array to generate a planar distribution of enhanced helicity density, with the same handedness at any point of the surface.

The organization of the paper is as follows. In Section II, we review the concept of helicity of electromagnetic fields as the chief quantity when dealing with chirality detection. In Sections III and IV, optical properties and helicity density content of nearfields, respectively, are investigated in proximity of both an individual and an array of high-density DNAs. Section V concludes our analysis.

II. Helicity of fields

It is shown that since linear and angular momenta of charged particles interacting with electromagnetic fields are conserved, a part of these quantities may transfer to electromagnetic fields and this leads to de-

¹ M.hanifeh@uci.edu

² F.capolino@uci.edu

fine similar mechanical quantities for classical electromagnetic fields²⁶. However, helicity as one of the conserved quantities for classical electromagnetic fields was first defined based on mathematical concepts rather than mechanical ones, in terms of quantified *knottedness* or *curliness* of a vector field²⁷. In this regard, helicity density for time harmonic electromagnetic fields reads^{27–29} (when using the International System of Units)

$$h = \frac{1}{4c_0} (\epsilon_0 \mathbf{F}^* \cdot \nabla \times \mathbf{F} + \mu_0^{-1} \mathbf{A}^* \cdot \nabla \times \mathbf{A}) \quad (1)$$

where \mathbf{A} and \mathbf{F} are, respectively, the magnetic and electric vector potentials related to the electric \mathbf{E} and magnetic \mathbf{H} fields via $\mathbf{E} = -\nabla \times \mathbf{F}$ and $\mathbf{H} = \mu_0^{-1} \nabla \times \mathbf{A}$. Moreover, c_0 , ϵ_0 and μ_0 are, respectively, the speed of light, permittivity, and permeability in vacuum, and the superscript “*” denotes complex conjugation. Note that fields with time dependence $\exp(-i\omega t)$, where ω is the angular frequency, are considered throughout the paper. Further investigations clarified the physical significance of helicity, and it was shown that the mathematical integration of h as defined in Eq.(1) over the whole space is indeed the classical limit of the difference between the number of right-handed and left-handed photons in the field²⁸. Helicity is also closely related to optical chirality, a quantitative measure of handedness of electromagnetic fields, introduced by Tang and Cohen to represent the strength of field in detection of chirality of matter^{5,6}. Indeed, for time-harmonic electromagnetic fields, the time-averaged optical chirality and helicity are proportional. Here, we adopt helicity as the measure to quantify fields’ chirality, i.e., their handedness, since it is shown that it is physically meaningful, rather than optical chirality²⁹.

After introduction of the chirality concept in electromagnetic fields and discussing its significance on chirality detection of matter, intensive research studies have been performed to propose structured lights, such as nearfields of NAs and optical beams, to enhance helicity density in comparison to plane waves with circular polarization^{14,19,22,25,30–33}. Helicity enhancement depends on several factors which become clear when we employ Coulomb gauge $\nabla \times \mathbf{A} = \mathbf{0}$ and $\nabla \times \mathbf{F} = \mathbf{0}$, and simplify Eq. (1) to

$$h = \frac{\Im\{\mathbf{E} \cdot \mathbf{H}^*\}}{2\omega c_0}. \quad (2)$$

Equation (2) shows that helicity is enhanced when: the magnitudes of electric and magnetic field components increase, their phase difference approaches $\pi/2$, and the electric field vector and the conjugate of the magnetic field vector become collinear. However, it has recently been proved that an upper-bound of helicity

density of an electromagnetic field exists and is proportional to its energy density³⁴. Fields which possess the maximum attainable helicity density are called *optimally chiral* and satisfy conditions

$$\mathbf{E} = \pm i\eta_0 \mathbf{H} \quad (3)$$

where η_0 denotes the intrinsic wave impedance of vacuum, and their helicity density takes the value of

$$h = \pm \frac{u}{\omega}, \quad (4)$$

where $u = (\epsilon_0 |\mathbf{E}|^2 + \mu_0 |\mathbf{H}|^2)/4$ is the time average energy density of the electromagnetic field. As discussed in³⁴, the helicity value in (4) constitutes the maximum (positive or negative) helicity any field with a given time average energy density u may have, hence it represents a universal bound. A simple example satisfying such relation that people have been using without realizing its full implication is the circularly polarized plane wave. Another example is the azimuthally-radially polarized beam (ARPB)^{10,15,35,36} used for example in Refs^{10,15,35} that is a composition of an azimuthally polarized beam (APB)^{37–41} and a radially polarized beam (RPB)^{36,42,43}.

Another remarkable example of optimally chiral fields, highly related to this paper, is the nearfield of a high-density dielectric (e.g. of Si or TiO₂) spherical particle with appropriate size and under suitable illuminations such as a Gaussian beam with circular polarization^{8,15}, and as an azimuthally-radially polarized beam used, respectively,¹⁵ which provides also helicity near-field enhancement with respect to that of an illuminating plane wave. In the following sections we discuss exactly that, i.e, helicity density enhancement in nearfield of a high-density DNA and in an array composed of DNAs.

III. Helicity Analysis of Nearfields of a high-density dielectric NA

As a determinant factor in the electromagnetic response of an array, we devote this section to investigate the interaction of a spherical high-density DNA with electromagnetic fields. Let us assume that a spherical DNA with radius a is located at the origin of the coordinate system and is irradiated by an incident field with electric and magnetic components \mathbf{E}_{inc} and \mathbf{H}_{inc} , respectively, propagating along the $+z$ direction in free space (Figure 1(a)). As a quantitative measure of the interaction between the DNA and the incident field, we employ the scattering cross section of the DNA denoted by σ_s , defined as the total scattered power normalized to the incident field irradiance⁴⁴. First, we employ a full wave simulation analysis based on the finite element method (FEM) implemented in CST Microwave

Studio⁴⁵ to obtain the DNA's σ_s , shown in Figure 1 (b), when it is irradiated by a plane wave with electric field $\mathbf{E}_{\text{inc}} = E_0 e^{ik_0 z} \hat{\mathbf{y}}$ versus wavelength within the interval of 600 nm to 800 nm, for various radii a . Here, E_0 is the complex amplitude of the electric field, and $\hat{\mathbf{x}}$ and $\hat{\mathbf{y}}$ are unit vectors of the Cartesian coordinate system. In this example in the following ones we assume that the high-density DNA is made of Silicon, whose refractive index is extracted from Ref.⁴⁶.

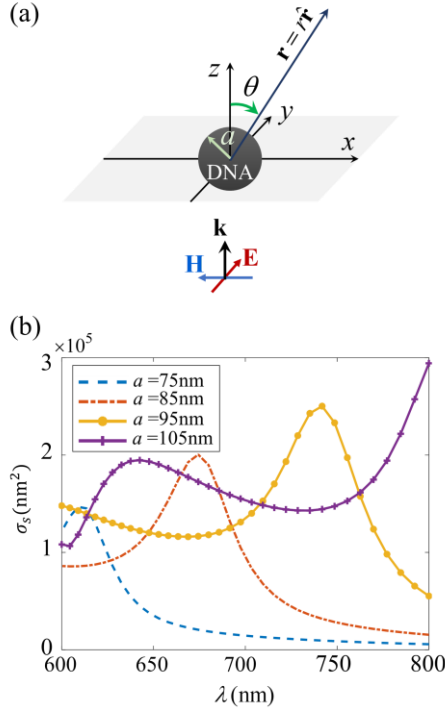


Figure 1. (a) High-density dielectric nanoantenna (DNA) with radius a located at the origin of a coordinate system and illuminated by a plane wave. (b) Scattering cross section σ_s of the DNA versus operating wavelength λ for four distinct sphere's radii. In this example and in all the following ones the DNA is made of Silicon. As it will be clear in the next figure, the peaks represent magnetic resonances.

As is clear from Figure 1, the scattering cross section σ_s depends on the radius, and the general trend is that larger particles provide higher σ_s values as expected. Furthermore, the wavelength of the peak of scattering cross section increases when the particle size increases. Although the total scattering cross section provides useful quantitative information about the interaction between the DNA and the incident field, it does not present any information about the nature of such an interaction. To elaborate the essence of the interaction, we model the DNA by induced electric \mathbf{p} and magnetic \mathbf{m} dipole moments and neglect the contributions from higher multipoles in the scattering. Such an approximate modeling is valid as long as the DNA is

optically small and has been widely used in metasurface design and analysis⁴⁷⁻⁵⁰. The dipole moments are related to the incident field $\mathbf{E}_{\text{inc}}^o$ and $\mathbf{H}_{\text{inc}}^o$ at the position of the DNA through

$$\begin{aligned} \mathbf{p} &= \alpha_{ee} \mathbf{E}_{\text{inc}}^o, \\ \mathbf{m} &= \alpha_{mm} \mathbf{H}_{\text{inc}}^o. \end{aligned} \quad (5)$$

Here, α_{ee} and α_{mm} are electric and magnetic polarizabilities, respectively, which encapsulate optical properties of the DNA and are determined by the DNA radius and its refractive index. (For the sake of clarity, the magnetic dipole is defined here as $\mathbf{m} = \frac{1}{2} \int \mathbf{r} \times \mathbf{J}(\mathbf{r}) dV$ where $\mathbf{J}(\mathbf{r})$ represents the displacement current density.) In what follows, without loss of generality we focus on a DNA with radius $a = 85$ nm made of Silicon with the peak of scattering cross section σ_s occurring at wavelength $\lambda = 675$ nm which is almost in the middle of the considered wavelength range. The magnitudes of electric and magnetic dipole polarizabilities of a DNA with radius $a = 85$ nm, and their phase difference $\Delta\varphi$ are calculated using the expressions from Mie theory and are plotted in Figure 2. This figure shows that at $\lambda = 730$ nm the electric and magnetic polarizabilities are approximately balanced, i.e., when $|\alpha_{ee}|/\epsilon_0 = |\alpha_{mm}|$ and their phase difference is very close to zero, which means that the Kerker condition⁵¹⁻⁵⁵ is almost satisfied at that wavelength and hence the DNA directs the scattered field in the forward direction (a source with zero back radiation is often referred to as Huygens source⁵⁶⁻⁵⁹).

The peak of α_{mm} at wavelength $\lambda = 675$ nm is often referred to as “magnetic resonance” of the DNA. The angular dependence of the differential scattering cross section, i.e., time-averaged power radiated per unit solid angle²⁶ normalized to the incident field power intensity, of the proposed DNA at $\lambda = 675$ nm and $\lambda = 730$ nm are illustrated in Figure 3 assuming a plane wave coming from the negative z direction and with electric field polarized along the y direction. (In other words, it represents the radiation pattern of the DNA, excited by the above mentioned plane wave.)

Results are calculated via full wave simulations. Note that the differential scattering cross section is calculated in the yz plane and θ is the angle between the z axis and the observation point (see Figure 1 (a)). As illustrated in Figure 2, at $\lambda = 730$ nm the Kerker condition is satisfied and the DNA scatters the dominant part of the power in the forward direction, i.e., along $\theta = 0$. However, at wavelength $\lambda = 675$ nm, which corresponds to the peak of scattering cross section σ_s in Figure 1, the DNA scatters isotropically in the yz plane because at this wavelength the DNA acts mainly as a magnetic dipole oriented along the x axis.

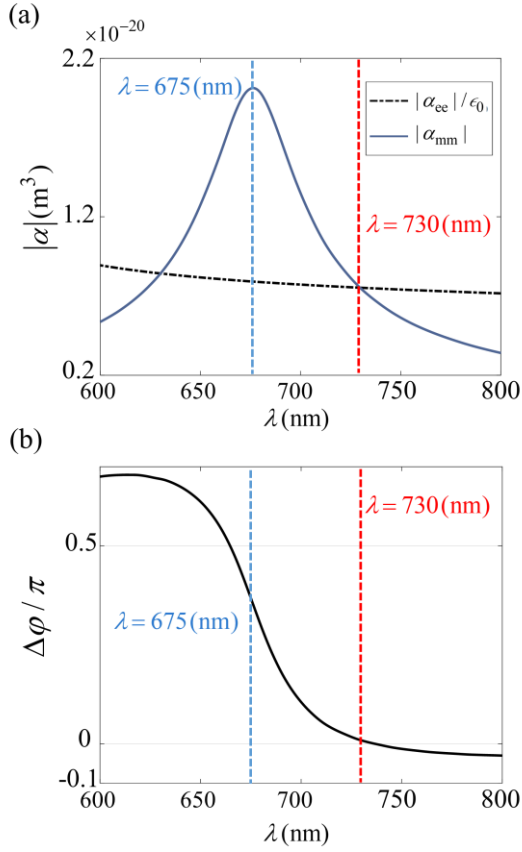


Figure 2. (a) Magnitude and (b) normalized phase difference between of the electric α_{ee} and magnetic α_{mm} dipole polarizabilities of a single DNA with radius $a=85$ nm made of Silicon. At $\lambda = 730$ nm, the Kerker condition⁵¹ is satisfied, i.e., the polarizabilities are balanced $|\alpha_{ee}|/\epsilon_0 = |\alpha_{mm}|$ and $\Delta\varphi = 0$.

This result indicates that an array composed of DNAs with radius $a = 85$ nm (to be investigated later in this paper) would mainly transmit all the incident power at $\lambda = 730$ nm which is advantageous when transmitted power is employed to detect chirality in accordance to standard circular dichroism experiments. However, coupling among the DNAs (and a possible phase difference between incident and scattered fields) would cause a wavelength shift for maximum transmittance to occur.

Next, in Figure 4 we compare the scattering cross section σ_s obtained from the full wave simulations and Mie theory considering only the electric and magnetic dipole moments, which reads^{26,60}

$$\sigma_s = \frac{\omega k_0^3 \eta_0}{6\pi\epsilon_0} (|\alpha_{ee}|^2 + \epsilon_0 |\alpha_{mm}|^2), \quad (6)$$

where $k_0 = \omega\sqrt{\epsilon_0\mu_0}$ is the vacuum wavenumber, to ensure that the dipolar approximation provides an accurate scattering description of the DNA.

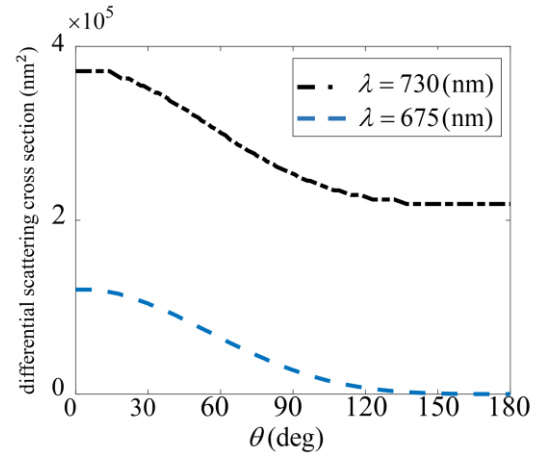


Figure 3. Angular dependence of differential scattering cross section of a single DNA with radius $a=85$ nm, in the yz plane, versus angle θ between the $+z$ axis and the observation point, calculated via full wave simulations. Here the DNA is illuminated by a plane wave polarized along y and propagating along the $+z$ direction. At $\lambda = 730$ nm the Kerker condition is satisfied and the DNA scatters light mainly in the forward direction. The wavelength of $\lambda = 675$ nm corresponds to the peak of the scattering cross section σ_s , and shows an isotropic scattering in the yz plane, because the DNA acts mainly as a magnetic dipole oriented along x .

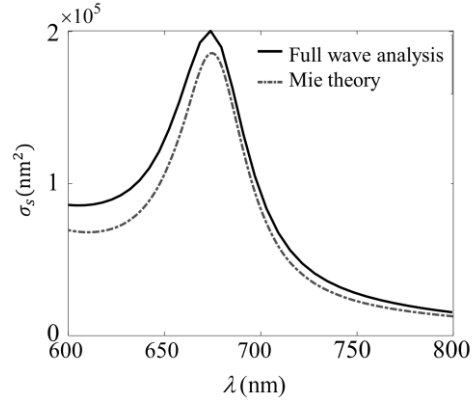


Figure 4. Agreement between the scattering cross section σ_s of a single DNA with radius $a=85$ nm obtained from Mie theory considering only the electric and magnetic dipole moments and from full wave simulation. This proves that considering only the two electric and magnetic dipole moments representing the DNA scattering is a valid approximation in the considered wavelength range.

Finally, since the upper bound of helicity density is linearly linked to the energy density as was shown in Ref.³⁴, in Figure 5 and Figure 6 we show the electric and magnetic energy densities in total nearfields of the DNA illuminated by a plane wave with electric field linearly polarized along the y direction, at $\lambda = 730$ nm.

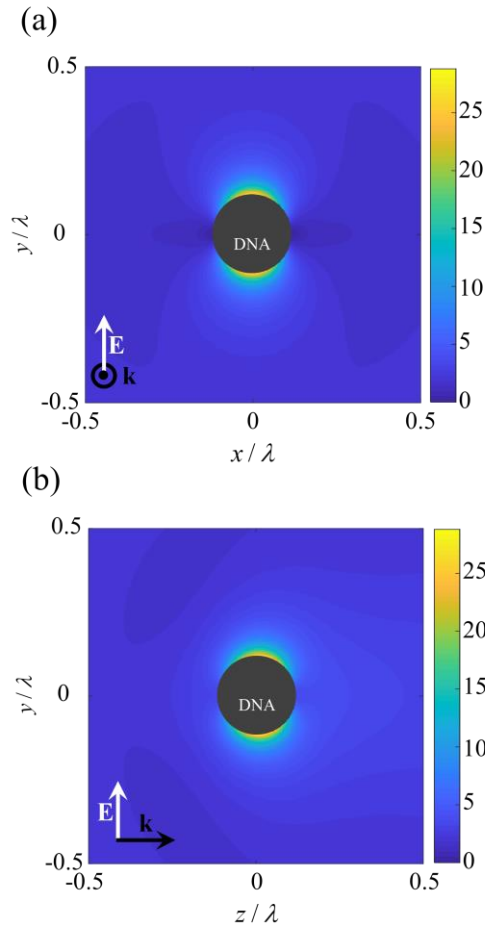


Figure 5. Distribution of total electric energy density, normalized to that of incident field, around a single DNA with radius $a = 85$ nm, in the (a) xy and (b) yz planes at $\lambda = 730$ nm. The electric dipole moment induced in the DNA by the incident field is oriented along the y direction; therefore, the total electric energy density takes its maximum enhancement along this axis.

To improve helicity density, it is required to simultaneously enhance electric and magnetic energy densities. However, according to Eq. (5), the induced electric \mathbf{p} and magnetic \mathbf{m} dipole moments are, respectively, oriented along the y and x axes when the DNA is illuminated by y -polarized (electric field) plane wave. Therefore, electric energy density is enhanced more effectively along the y axis while the maximum of magnetic energy density occurs along the x axis.

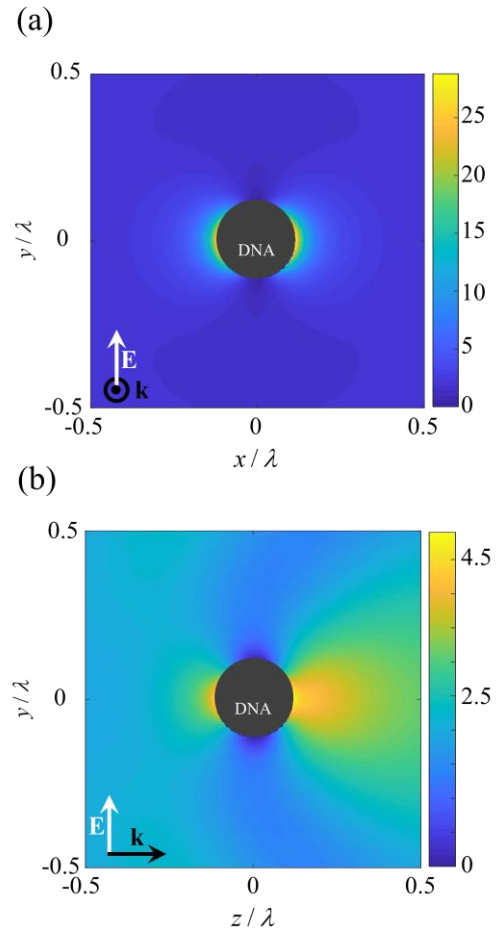


Figure 6. Distribution of the magnetic energy density, normalized to that of the incident field, around a single DNA with radius $a = 85$ nm, in the (a) xy and (b) yz planes at $\lambda = 730$ nm. Magnetic dipole moment is oriented along x axis and magnetic energy density takes its maximum enhancement along this axis.

Moreover, since the incident field and DNA is achiral, and helicity is a conserved quantity, helicity distribution of the total field around the DNA oscillates between positive and negative values and averages to zero. Therefore, nearfields of a DNA illuminated by a linearly polarized plane wave is not a suitable candidate to improve chirality detection since helicity density would not have the same positive or negative sign (handedness) in all regions of space near the DNA. In the following subsection, we analyze helicity density of the total nearfields of a DNA illuminated by a plane wave with circular polarization and show that helicity has a single sign (handedness).

A. Analysis of helicity density of nearfields of a DNA illuminated by a plane wave with circular polarization

We illuminate a single DNA made of Si with radius $a=85$ nm by a right handed circularly polarized plane wave with electric field \mathbf{E}_{inc} represented as

$$\mathbf{E}_{\text{inc}} = E_0(\hat{\mathbf{x}} + i\hat{\mathbf{y}})e^{ik_0z}/\sqrt{2}, \quad (7)$$

propagating along the $+z$ axis and magnetic field $\mathbf{H}_{\text{inc}} = (E_0/\eta_0)(\hat{\mathbf{y}} - i\hat{\mathbf{x}})e^{ik_0z}/\sqrt{2}$ is obtained from Maxwell equation $\mathbf{H} = (i\omega\mu_0)^{-1}\nabla \times \mathbf{E}$.

Here and in the following a hat tags unit vectors. It has been shown that helicity density h of the total field around a DNA is the sum of the helicity density of the incident field h_{inc} , the helicity density of the scattered field h_{sca} , and an interference helicity density h_{int} ¹⁵, i.e.,

$$h = h_{\text{inc}} + h_{\text{int}} + h_{\text{sca}} \quad (8)$$

The sign of helicity density of the circularly polarized incident field is positive based on the definition in Eq. (2). Scattering helicity density h_{sca} at location $\mathbf{r} = r\hat{\mathbf{r}}$, generated by a DNA in its surrounding, when the DNA's scattering is represented by only dipole moments \mathbf{p} and \mathbf{m} is approximated by the expression¹⁵

$$h_{\text{sca}} \approx \frac{\eta_0}{32\pi^2\omega r^6} \Im\{3(\hat{\mathbf{r}} \cdot \mathbf{p})(\hat{\mathbf{r}} \cdot \mathbf{m}^*) + \mathbf{p} \cdot \mathbf{m}^*\}. \quad (9)$$

after keeping only terms with dependence r^{-3} and ignoring those which depend on r^{-1} and r^{-2} . Introducing Eqs. (5) and (7) into Eq.(9) simplifies the expression of scattering helicity density h_{sca} to

$$h_{\text{sca}} \approx \frac{\epsilon_0|E_0|^2}{32\pi^2\omega r^6} \left(\frac{3}{2}\sin^2\theta + 1\right) \Re\{\alpha_{\text{ee}}\alpha_{\text{mm}}^*\} / \epsilon_0, \quad (10)$$

where θ is the polar angle in spherical coordinate system (r, θ, φ) . Figure 7 shows the term $\Re\{\alpha_{\text{ee}}\alpha_{\text{mm}}^*\} / \epsilon_0$ in Equation (10) which relates the scattering helicity density to the electric and magnetic polarizabilities of the DNA. Besides the slow varying $1/\omega$ term in (11), it is $\Re\{\alpha_{\text{ee}}\alpha_{\text{mm}}^*\} / \epsilon_0$ that controls the maximum of the scattering helicity density. Note that helicity enhancement, i.e., normalized scattering helicity density h_{sca} to that of the incident field $h_{\text{inc}} = \epsilon_0|E_0|^2/(2\omega)$, is independent from amplitude and angular frequency of the excitation and is proportional to $h_{\text{sca}}/h_{\text{inc}} \propto \Re\{\alpha_{\text{ee}}\alpha_{\text{mm}}^*\} / \epsilon_0$. Therefore, since this term, as depicted in Figure 7, does not drop dramatically, the discussed DNA provides enhanced helicity density over a wide wavelength range between 700 nm and 800 nm.

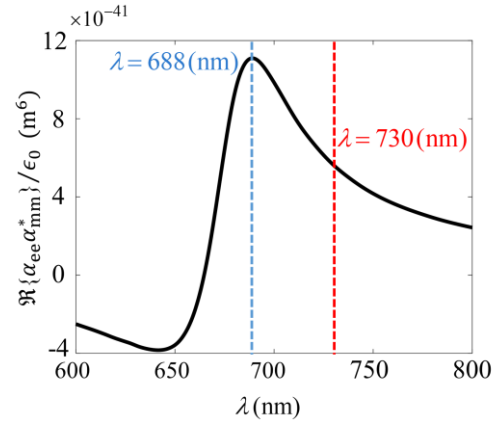


Figure 7. Term $\Re\{\alpha_{\text{ee}}\alpha_{\text{mm}}^*\}/\epsilon_0$, which is proportional to $h_{\text{sca}}/h_{\text{inc}}/\epsilon_0$, for a single DNA with radius $a=85$ nm versus wavelength. This term takes its maximum around $\lambda = 688$ nm, while it has a lower value at $\lambda = 730$ nm where polarizabilities are balanced.

Figure 7 shows that the scattering helicity density generated by a DNA illuminated by a plane wave with CP reaches its maximum around $\lambda = 688$ nm while its value is smaller at $\lambda = 730$ nm where the two polarizabilities are balanced (when $\alpha_{\text{ee}} = \epsilon_0\alpha_{\text{mm}}$). In Ref.¹⁵ it is proved that balanced polarizabilities (when $\alpha_{\text{ee}}/\epsilon_0 = \alpha_{\text{mm}}$) are required to generate optimally chiral fields around a DNA, when it is illuminated by an optimally chiral incident field satisfying condition (3) such as a plane wave with circular polarization. This means that the maximum of helicity density does not corresponds to the “optimal chiral condition”. However, for applications which require optimally chiral fields, such as chirality characterization of nanoparticles, this condition is satisfied at expense of losing a portion of helicity enhancement. Note that as discussed earlier in this paper, balanced polarizabilities also correspond to satisfaction of Kerker condition which is advantageous for applications such as CD experiments where measuring the transmitted power through an array of discussed DNAs is the goal.

Since the incident field has a right-handed circular polarization, the term h_{inc} has positive value. Therefore, incident and scattering helicity densities interfere constructively contributing to a higher total helicity density at wavelength where $\Re\{\alpha_{\text{ee}}\alpha_{\text{mm}}^*\} / \epsilon_0$ takes positive values. Figure 8 illustrates the distribution of total helicity density (of the total field), obtained from full wave simulations, normalized to that of incident field in the transverse xy plane, at $\lambda = 730$ nm.

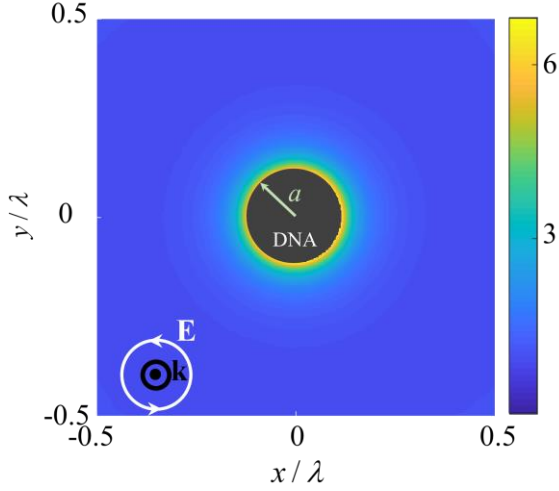


Figure 8. Normalized helicity density to that of the incident field around a single DNA with radius $a = 85$ nm, irradiated by a plane wave with circular polarization at $\lambda = 730$ nm, in xy plane, i.e., at $\theta = \pi/2$. Since illumination has circular polarization the distribution is symmetric in the azimuthal plane.

This figure shows that helicity of the total field is distributed symmetrically and with uniform handedness around the DNA in the transverse xy plane, which is in accordance with Eq.(10). Note that helicity is enhanced by a factor of 6.3 on the surface of the DNA and drops to half of this value (enhancement of 3.2) at a distance of 20 nm, approximately equal to 0.03λ . Moreover, condition (3) is satisfied for fields in the xy plane and energy density takes a distribution similar to that of helicity density illustrated in Figure 8. Although helicity density decreases along the radial direction away from the DNA, helicity density of the total field normalized to the product of the energy density and angular frequency, i.e., $h/(u\omega)$, depicted in Figure 9 does not decrease and assumes a value of unity which shows that fields around such DNA is optimally chiral.

According to Eq.(10), the helicity density of the scattered field h_{sca} drops fast with a factor of r^{-6} since it is mainly due to the nearfield. Moreover, as discussed in Ref. ¹⁵ interference helicity density h_{int} , i.e., the second term in Eq.(8), drops by a factor of r^{-3} . Therefore, total helicity density enhancement defined as h/h_{inc} tends to unity as $1 + h_{int}/h_{inc} + h_{sca}/h_{inc}$. Therefore, to provide enhanced helicity density over a broader area, we propose an array of DNAs to enhance helicity over a surface in proximity of the array.

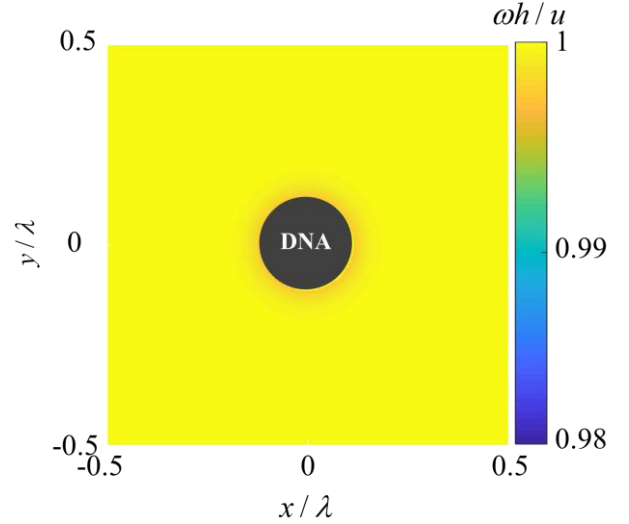


Figure 9. Helicity density normalized to the product of energy density and angular frequency, i.e., $h/(u\omega)$ around a single DNA with radius $a=85$ nm in the xy plane at wavelength $\lambda=730$ nm. This quantity equals unity for optimally chiral fields and fields whose $h/(u\omega)$ values are close to unity are close to satisfying the required conditions to be optimally chiral.

IV. Helicity Analysis of a planar Array of DNAs

In this section we show how the helicity density distribution over the surface of a planar array composed of DNAs as in Figure 10, illuminated by a plane wave with circular polarization, is enhanced all over the array surface, paving the way of using such metasurfaces for chirality detection of nanoparticles. First, to investigate the influence of DNAs' size and periodicity on array's functionality, we irradiate the array by a plane wave with linear polarization and normal incidence and calculate the field reflection and transmission coefficients R and T defined, respectively, as the amplitude of the reflected and transmitted tangential component of the electric field normalized to that of the illumination. Next, we analyze helicity density of the field in between the arrayed DNAs at the specific wavelength corresponding to almost full transmission. Full wave simulations are carried out by using the frequency domain finite element method module in the software package CST Studio Suite by DS SIMULIA. Floquet boundary condition is imposed on boundaries of the array's unit cell and Floquet modes up to first order are considered.

Note that homogenization of a metasurface parameters, which is employed in analysis of metasurfaces with elements sufficiently small compared to the operating wavelength, is not needed in the analysis of the array we consider in this section ^{48,60,61}.

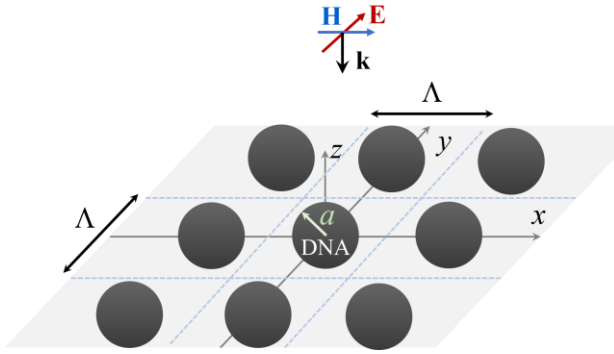


Figure 10. Array of DNAs with radius a arranged in the xy plane with period Λ , illuminated by a plane wave, propagating along the negative z direction.

The properties of a DNA array as that in Figure 10 are determined by the resonance frequency of the DNA, which is dictated by its radius a , and the periodicity of the array Λ , which influences the interaction between array elements. Here we mainly study arrays composed of DNAs with radius $a = 85$ nm, however to examine how the functionality of the array is affected by the DNAs radius a , we calculate the transmission and reflection coefficients for three distinct values of radius a , using full wave simulations, when the array is irradiated by a plane wave with linear polarization propagating along the negative z direction. (A subsection later in the paper is devoted to helicity analysis of the array when it is illuminated by plane waves with circular polarization.)

Figure 11 depicts the magnitude of the field reflection R and transmission T coefficients of the array with periodicity parameter $\Lambda = 270$ nm for three distinct radii a of the DNA. This figure shows that the array transmits almost the total power of the incident field at the wavelength where the Kerker condition is satisfied⁵¹, for each case, not at the wavelength at which the scattering cross section σ_s of a single DNA takes its maximum (see Figure 2), though it is not far from that.

The field reflection R and transmission T coefficients of the array of DNAs with radius $a = 85$ nm for three distinct periodicity parameters Λ is depicted in Figure 12. As it is clear from this figure, the null in the reflection coefficient R does not dramatically change with period length Λ and it approximately (note a small shift in the wavelength of the null) occurs at wavelength $\lambda = 730$ nm, where the Kerker condition⁵¹ is satisfied for individual DNA inclusions with radius $a = 85$ nm. A zero transmission occurs at wavelengths in the range $600 \text{ nm} < \lambda < 650 \text{ nm}$ for the cases considered.

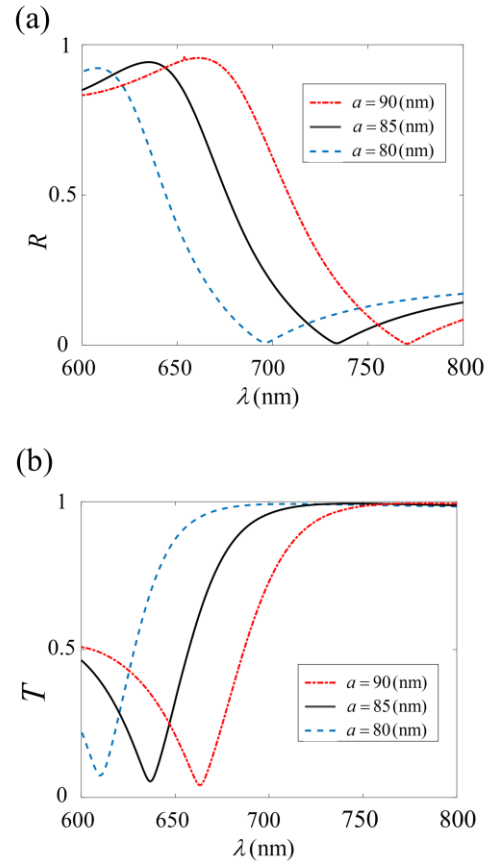


Figure 11. Magnitude of field transmission T (a) and reflection R (b) coefficients for an array of high-density DNAs with $\Lambda = 270$ nm illuminated by a plane wave polarized along y axis and propagating along the negative z direction. At the wavelength where the Kerker condition⁵¹ is satisfied the array is fully transmissive.

By looking at both Figs. 11 and 12 we conclude that the peak of transmission coefficient T is a mixed behavior impacted by both the array period Λ and the inclusions' sizes a since by increasing Λ or by increasing a this peak wavelength is red shifted.

At this step, as a practical exercise, we examine the impact of a glass substrate on the reflection and transmission coefficients of the proposed DNA array. Therefore, in the following we consider the array just above a glass substrate with refractive index $n = 1.5$ and thickness $d = 1 \mu\text{m}$. Figure 13 represents the magnitude of the field reflection R and transmission T coefficients of the array illuminated by a plane wave polarized along the y direction and propagating along the negative z direction.

The minimum of the reflection coefficient R (around $\lambda = 700$ nm) is slightly red shifted with respect to the null of R when the array is floating in free space.

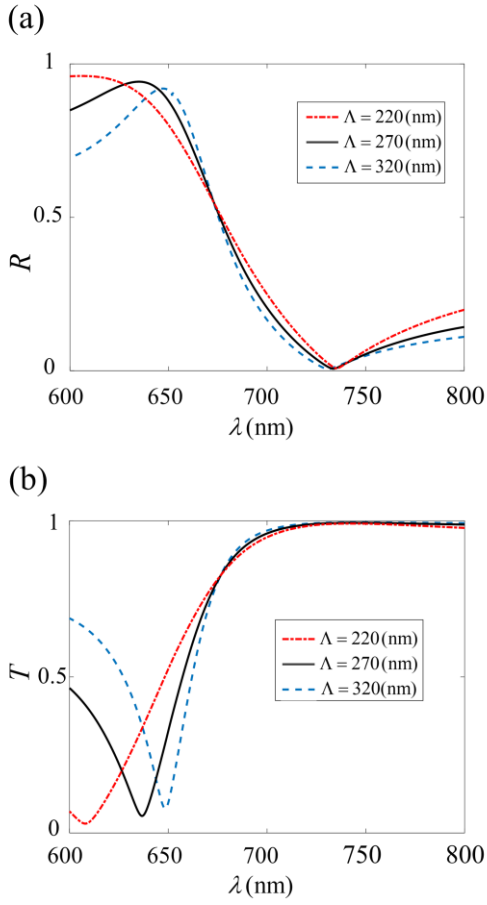


Figure 12. Magnitude of field reflection R (a) and transmission T (b) coefficients of an array of high-density DNAs with radius $a=85\text{nm}$ for three distinct periods Λ . Reflection R is not sensitive to change in periodicity Λ and takes its minimum value at $\lambda = 730\text{ nm}$ where Kerker condition⁵¹ is satisfied for a single DNA.

However, the array still transmits most of the incident power at $\lambda = 730\text{ nm}$, and therefore, its operation is weakly affected by presence of the glass substrate. This is because the DNA are mainly in air (above the substrate) and the contrast between the glass substrate and the air is not high and hence the scattered fields by DNAs remain quite similar to the case without substrate. Therefore, in what follows, and for the sake of simplicity in full wave simulations, we consider the proposed DNA array in free space.

Next, we analyze helicity density at a surface $z = 0$ of the array at the wavelength where the field reflection coefficient R takes its minimum value (i.e., maximum transmission) and demonstrate that an array of DNAs is a convenient candidate to improve chirality detection in CD experiments when used as a substrate for chiral samples.

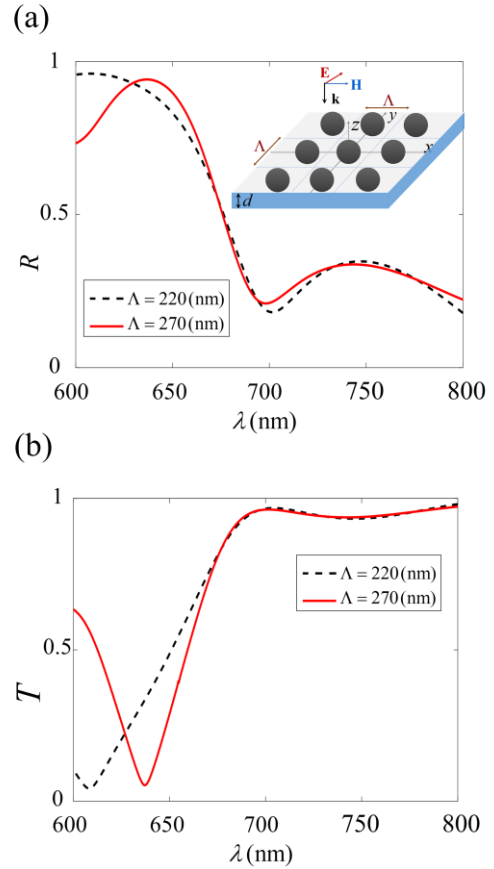


Figure 13. Magnitude of the field reflection R (a) and transmission T (b) coefficients for an array of high-density DNAs with radius $a=85\text{ nm}$ on a glass substrate illuminated by a plane wave linearly polarized along y and propagating along the negative z direction, for two distinct periods Λ . The substrate has a refractive index $n=1.5$ and thickness $d = 1\mu\text{m}$.

A. Helicity enhancement of an array of DNAs illuminated by a plane wave with circular polarization

In this subsection we examine the ability of the proposed array of DNAs to enhance helicity density with respect to that of an incident circularly polarized wave. As discussed earlier, when the Kerker condition (for a single DNA) is satisfied, the reflection R and transmission T coefficients of the array are chiefly affected by the radius of the DNAs, whereas the periodicity parameter Λ does not significantly shift the, the maximum transmission's wavelength. However, when the periodicity parameter Λ is reduced, the distance between DNAs decreases. Therefore, energy density is localized in hot spots formed in spaces between DNAs and the upper bound of helicity density which is linearly linked to energy density also increases. In Figure 14 we show the total helicity density at the surface $z = 0$, normalized to that of the incident field, for two distinct array periods of $\Lambda = 220\text{ nm}$ and $\Lambda = 190\text{ nm}$.

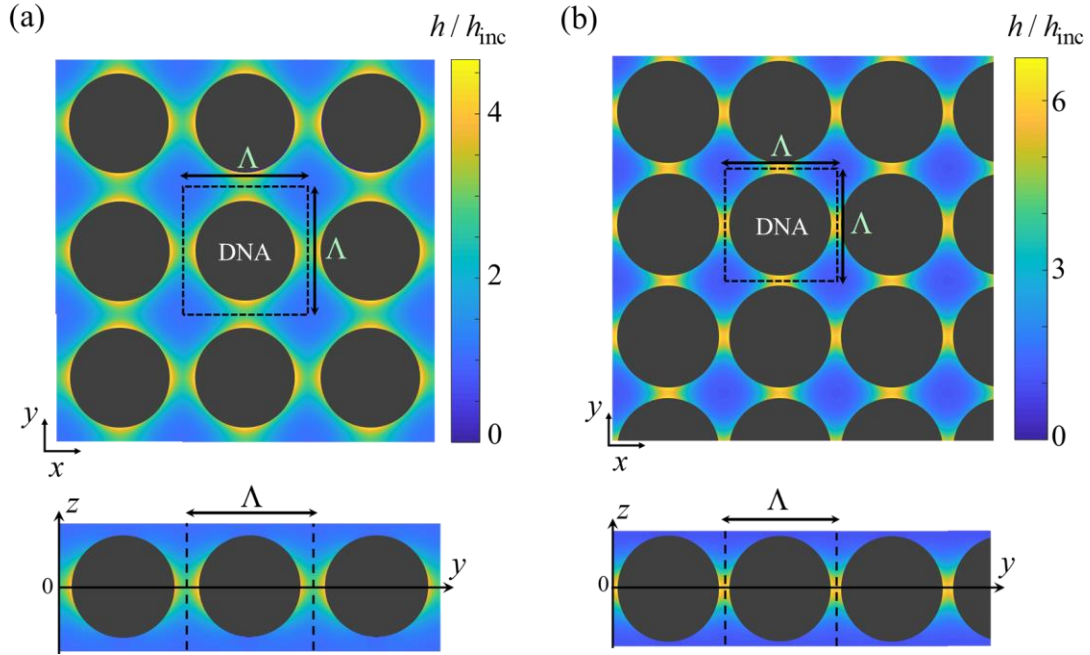


Figure 14. Helicity enhancement, i.e., helicity density of an array of high-density DNAs, with radius $a = 85\text{nm}$ made of Si, normalized to that of the incident field, on two array cross sections made of the xy plane (at $z = 0$), and in the yz plane, respectively, for periodicity parameters of (a) $\Lambda = 220\text{ nm}$, and (b) $\Lambda = 190\text{ nm}$ at wavelength $\lambda = 730\text{ nm}$. Note the different scale, and the higher helicity for the case with period $\Lambda = 190\text{ nm}$.

This figure shows that the array with smaller periodicity parameter Λ offers higher helicity enhancement in the hot spots formed between DNAs. In particular, observing helicity enhancement on the $z=0$ plane, along a line parallel to the x axis, crossing the center of the DNAs, one can observe that for arrays with periodicity $\Lambda = 220\text{ nm}$ and $\Lambda = 190\text{ nm}$ such enhancement drops, respectively, to 80 and 90 percent of their values on the surface of the DNA at a distance approximately equal to 0.015λ away from the surface of the DNA. This shows that the uniformity of helicity enhancement increases in the x and y directions when the periodicity decreases. Note that helicity enhancement around a *single* DNA that was depicted in Figure 8, drops approximately to 75 and 50 percent of its value on the surface of the DNA, respectively, at a distance equal to 0.015λ and 0.03λ away from the surface of the DNA. This shows that an array of Si DNA provides a helicity enhancement almost similar to that around a single DNA, but with better uniform distribution. Indeed, the array arrangement of DNAs spatially extends the enhanced helicity density over a large surface which is advantageous in some applications. Note that helicity densities illustrated in Figure 14 possess the same handedness over the whole $z=0$ surface and also off the $z=0$ surface. This latter aspect is particularly important since all over

such surface there are no fields with opposite handedness that could compromise the detection of chirality particles.

As discussed in Section II, the field around a *single* DNA with radius $a=85\text{ nm}$ at wavelength $\lambda=730\text{ nm}$, are *optimally chiral* when helicity and energy densities satisfy Eq. (4). Here, we illustrate the same concept for an array of DNAs. In Figure 15 we show helicity density normalized to the product of energy density and angular frequency, i.e., we show $h/(u\omega)$ (which equals unity for optimally chiral fields) at the surface $z=0$ of a unit cell of the array, in the xy plane. Figure 15 shows that when the periodicity of the array decreases, fields deviate from the required condition (3), so they are less optimally chiral.

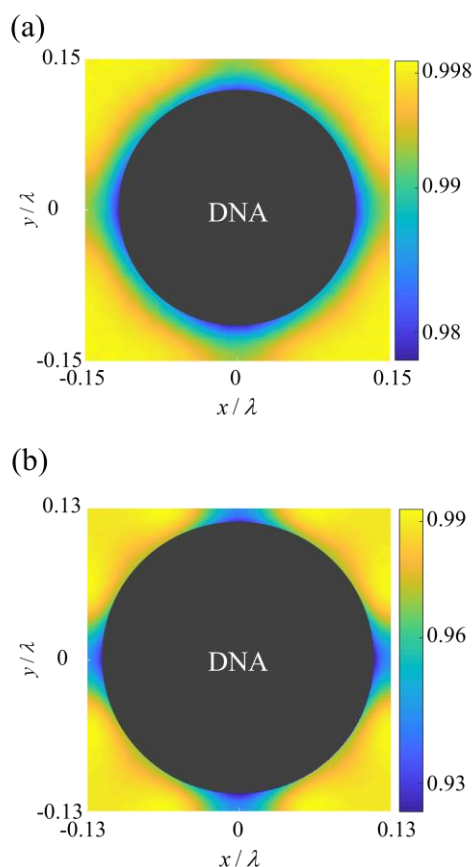


Figure 15. Plot of $h/(u\omega)$, i.e., of total helicity density normalized to the product of energy density and angular frequency, generated by an array of high-density DNAs with radius $a=85$ nm. We show such quantity in the xy plane (at $z=0$) over a unit cell of the array with period (a) $\Lambda = 220$ nm, and (b) $\Lambda = 190$ nm. This quantity equals ± 1 for optimally chiral fields, and this plot shows that the field in the DNA array is close to that limit.

V. CONCLUSION

We have shown that helicity density is enhanced and has the same handedness over the surface of an array composed of spherical high-density dielectric nanoantennas illuminated by a plane wave with circular polarization. First, we have investigated helicity density in the nearfield of a single DNA with balanced electric and magnetic polarizabilities, irradiated by a plane wave with circular polarization and discussed how the DNA's scattered field is optimally chiral³⁴. Helicity density is enhanced with a factor of 6.3 in vicinity of a single DNA, symmetrically in the plane transverse to the propagation direction of the incident field. However, helicity density of the scattered fields drops quickly moving away from the surface of a single DNA. Therefore, in the second part of the paper we have shown how helicity is enhanced over a surface of an array of DNAs. Moreover, our analysis shows that the nearfield over the surface of the array approximately satisfies the optimally chiral condition (3). The field slightly deviates from this optimal condition when

the inter-particle distances decreases but it generates a high helicity enhancement over a surface, with the same helicity handedness. This may present significant advantages in the detection of chirality of substances at surface level instead of in the bulk.

ACKNOWLEDGMENTS

The authors are thankful for the support from the W. M. Keck Foundation, USA. The authors acknowledge fruitful discussions with Dr. Mohammad Albooyeh, University of California Irvine. Finally, the authors are thankful to DS SIMULIA for providing CST Studio Suite that was instrumental in this study.

REFERENCES

- 1 J.P. Riehl, *Mirror-Image Asymmetry: An Introduction to the Origin and Consequences of Chirality* (John Wiley & Sons, 2011).
- 2 G.H. Wagnière, *On Chirality and the Universal Asymmetry: Reflections on Image and Mirror Image* (John Wiley & Sons, 2008).
- 3 R.J. Crossley, *Chirality and Biological Activity of Drugs* (CRC Press, 1995).
- 4 D.B. Amabilino, *Chirality at the Nanoscale: Nanoparticles, Surfaces, Materials and More* (John Wiley & Sons, 2009).
- 5 Y. Tang and A.E. Cohen, *Phys. Rev. Lett.* **104**, 163901 (2010).
- 6 Y. Tang and A.E. Cohen, *Science* **332**, 333 (2011).
- 7 Y. Zhao, A.N. Askarpour, L. Sun, J. Shi, X. Li, and A. Alù, *Nat. Commun.* **8**, 14180 (2017).
- 8 M. Hanifeh, M. Albooyeh, and F. Capolino, in *Complex Light Opt. Forces XIII* (International Society for Optics and Photonics, 2019), p. 1093504.
- 9 A. Hayat, J.P.B. Mueller, and F. Capasso, *Proc. Natl. Acad. Sci.* **112**, 13190 (2015).
- 10 M. Kamandi, M. Albooyeh, M. Veysi, M. Rajaei, J. Zeng, H.K. Wickramasinghe, and F. Capolino, *ACS Photonics* **5**, 4360 (2018).
- 11 G. Pellegrini, M. Finazzi, M. Celebrano, L. Duò, and P. Biagioni, *Chirality* **30**, 883 (2018).
- 12 M. Oksanen and A. Hujanen, in *1992 22nd Eur. Microwave Conf.* (1992), pp. 195–199.
- 13 A.O. Govorov, Z. Fan, P. Hernandez, J.M. Slocik, and R.R. Naik, *Nano Lett.* **10**, 1374 (2010).
- 14 A. García-Etxarri and J.A. Dionne, *Phys. Rev. B* **87**, 235409 (2013).
- 15 M. Hanifeh, M. Albooyeh, and F. Capolino, *Eprint ArXiv180904117* (2018).
- 16 M. Rajaei, J. Zeng, M. Albooyeh, M. Kamandi, M. Hanifeh, F. Capolino, and H.K. Wickramasinghe, *ACS Photonics* (2019).
- 17 J. Zeng, M. Kamandi, M. Darvishzadeh-Varcheie, M. Albooyeh, M. Veysi, C. Guclu, M. Hanifeh, M. Rajaei, E.O. Potma, H.K. Wickramasinghe, and F. Capolino, *EPJ Appl. Metamaterials* **5**, 7 (2018).
- 18 C.-S. Ho, A. Garcia-Etxarri, Y. Zhao, and J. Dionne, *ACS Photonics* **4**, 197 (2017).

- ¹⁹ B. Auguie, J.L. Alonso-Gómez, A. Guerrero-Martínez, and L.M. Liz-Marzán, *J. Phys. Chem. Lett.* **2**, 846 (2011).
- ²⁰ A.O. Govorov and Z. Fan, *ChemPhysChem* **13**, 2551 (2012).
- ²¹ D. Lin and J.-S. Huang, *Opt. Express* **22**, 7434 (2014).
- ²² V.K. Valev, J.J. Baumberg, C. Sibilía, and T. Verbiest, *Adv. Mater.* **25**, 2517 (2013).
- ²³ M. Schäferling, D. Dregely, M. Hentschel, and H. Giessen, *Phys. Rev. X* **2**, 031010 (2012).
- ²⁴ M. Schäferling, X. Yin, N. Engheta, and H. Giessen, *ACS Photonics* **1**, 530 (2014).
- ²⁵ M.H. Alizadeh and B.M. Reinhard, *ACS Photonics* **2**, 361 (2015).
- ²⁶ J.D. Jackson, *Classical Electrodynamics, 3rd Edition* (1998).
- ²⁷ A.F. Rana, *Eur. J. Phys.* **13**, 70 (1992).
- ²⁸ J.L. Trueba and A.F. Rañada, *Eur. J. Phys.* **17**, 141 (1996).
- ²⁹ R.P. Cameron, S.M. Barnett, and A.M. Yao, *New J. Phys.* **14**, 053050 (2012).
- ³⁰ F. Graf, J. Feis, X. Garcia-Santiago, M. Wegener, C. Rockstuhl, and I. Fernandez-Corbaton, *ACS Photonics* (2019).
- ³¹ V.E. Ferry, J.M. Smith, and A.P. Alivisatos, *ACS Photonics* **1**, 1189 (2014).
- ³² N.A. Abdulrahman, Z. Fan, T. Tonooka, S.M. Kelly, N. Gadegaard, E. Hendry, A.O. Govorov, and M. Kadodwala, *Nano Lett.* **12**, 977 (2012).
- ³³ X. Tian, Y. Fang, and M. Sun, *Sci. Rep.* **5**, (2015).
- ³⁴ M. Hanifeh, M. Albooyeh, and F. Capolino, *ArXiv1809 Phys.* (n.d.).
- ³⁵ J.S. Eismann, M. Neugebauer, and P. Banzer, *Optica* **5**, 954 (2018).
- ³⁶ A. Holleczeck, A. Aiello, C. Gabriel, C. Marquardt, and G. Leuchs, *Opt. Express* **19**, 9714 (2011).
- ³⁷ M. Veysi, C. Guclu, and F. Capolino, *JOSA B* **33**, 2265 (2016).
- ³⁸ C. Guclu, M. Veysi, and F. Capolino, *ACS Photonics* **3**, 2049 (2016).
- ³⁹ J. Zeng, F. Huang, C. Guclu, M. Veysi, M. Albooyeh, H.K. Wickramasinghe, and F. Capolino, *ACS Photonics* **5**, 390 (2018).
- ⁴⁰ M. Rajaei, M.A. Almajhadi, J. Zeng, and H.K. Wickramasinghe, *Opt. Express* **26**, 26365 (2018).
- ⁴¹ J. Zeng, M. Darvishzadeh-Varcheie, M. Albooyeh, M. Rajaei, M. Kamandi, M. Veysi, E.O. Potma, F. Capolino, and H.K. Wickramasinghe, *ACS Nano* **12**, 12159 (2018).
- ⁴² R. Oron, S. Blit, N. Davidson, A.A. Friesem, Z. Bomzon, and E. Hasman, *Appl. Phys. Lett.* **77**, 3322 (2000).
- ⁴³ H. Rubinsztein-Dunlop, A. Forbes, M.V. Berry, M.R. Dennis, D.L. Andrews, Masud Mansuripur, C. Denz, C. Alpmann, P. Banzer, T. Bauer, E. Karimi, Lorenzo Marrucci, M. Padgett, M. Ritsch-Marte, N.M. Litchinitser, N.P. Bigelow, C Rosales-Guzmán, A. Belmonte, J.P. Torres, T.W. Neely, M. Baker, R. Gordon, A.B. Stilgoe, J. Romero, A.G. White, R. Fickler, A.E. Willner, G. Xie, Benjamin McMorrán, and A.M. Weiner, *J. Opt.* **19**, 013001 (2017).
- ⁴⁴ C.F. Bohren and D.R. Huffman, *Absorption and Scattering of Light by Small Particles* (John Wiley & Sons, 2008).
- ⁴⁵ CST Studio Suite – EM Simulation Software. [Online]. Available: <https://www.cst.com/company> (2018).
- ⁴⁶ D.E. Aspnes and A.A. Studna, *Phys. Rev. B* **27**, 985 (1983).
- ⁴⁷ T. Niemi, A.O. Karilainen, and S.A. Tretyakov, *IEEE Trans. Antennas Propag.* **61**, 3102 (2013).
- ⁴⁸ M. Albooyeh, S. Tretyakov, and C. Simovski, *Ann. Phys.* **528**, 721 (2016).
- ⁴⁹ M.A. Salem and C. Caloz, *Opt. Express* **22**, 14530 (2014).
- ⁵⁰ M. Safari, A. Abdolali, H. Kazemi, M. Albooyeh, M. Veysi, and F. Capolino, in *2017 IEEE Int. Symp. Antennas Propag. Usn. Natl. Radio Sci. Meet.* (2017), pp. 1499–1500.
- ⁵¹ M. Kerker, D.-S. Wang, and C.L. Giles, *J. Opt. Soc. Am.* **73**, 765 (1983).
- ⁵² J.Y. Lee, A.E. Miroshnichenko, and R.-K. Lee, *Phys. Rev. A* **96**, 043846 (2017).
- ⁵³ X. Zambrana-Puyalto, I. Fernandez-Corbaton, M.L. Juan, X. Vidal, and G. Molina-Terriza, *Opt. Lett.* **38**, 1857 (2013).
- ⁵⁴ M. Nieto-Vesperinas, R. Gomez-Medina, and J.J. Saenz, *J. Opt. Soc. Am. A* **28**, 54 (2011).
- ⁵⁵ B.S. Luk'yanchuk, N.V. Voshchinnikov, R. Paniagua-Domínguez, and A.I. Kuznetsov, *ACS Photonics* **2**, 993 (2015).
- ⁵⁶ A.I. Kuznetsov, A.E. Miroshnichenko, M.L. Brongersma, Y.S. Kivshar, and B. Luk'yanchuk, *Science* **354**, aag2472 (2016).
- ⁵⁷ M.F. Picardi, A.V. Zayats, and F.J. Rodríguez-Fortuño, *Phys. Rev. Lett.* **120**, 117402 (2018).
- ⁵⁸ R. Dezert, P. Richetti, and A. Baron, *Phys. Rev. B* **96**, (2017).
- ⁵⁹ Y.H. Fu, A.I. Kuznetsov, A.E. Miroshnichenko, Y.F. Yu, and B. Luk'yanchuk, *Nat. Commun.* **4**, 1527 (2013).
- ⁶⁰ S. Tretyakov, *Analytical Modeling in Applied Electromagnetics* (Artech House, 2003).
- ⁶¹ M. Albooyeh, *Electromagnetic Characterization of Metasurfaces*, PhD thesis, Aalto University, 2015.